Physics of Fluids

Droplet impact on immiscible liquid pool: Multi-scale dynamics of entrapped air cushion at short timescales

Cite as: Phys. Fluids **34**, 052004 (2022); https://doi.org/10.1063/5.0091584
Submitted: 16 March 2022 • Accepted: 25 April 2022 • Published Online: 09 May 2022

Durbar Roy, Sophia M, Srinivas S. Rao, et al.

Physics of Fluids ARTICLE scitation.org/journal/phf

Droplet impact on immiscible liquid pool: Multi-scale dynamics of entrapped air cushion at short timescales

Cite as: Phys. Fluids **34**, 052004 (2022); doi: 10.1063/5.0091584
Submitted: 16 March 2022 · Accepted: 25 April 2022 ·
Published Online: 9 May 2022

Durbar Roy, Sophia M, Srinivas S. Rao, and Saptarshi Basu[a)]

AFFILIATIONS

Department of Mechanical Engineering, Indian Institute of Science, Bengaluru, Karnataka 560012, India

[a)]Author to whom correspondence should be addressed: sbasu@iisc.ac.in

ABSTRACT

We have detected unique hydrodynamic topology in thin air film surrounding the central air dimple formed during drop impact on an immiscible liquid pool. The pattern resembles spinodal and finger-like structures typically found in various thin condensed matter systems. However, similar structures in thin entrapped gas films during drop impacts on solids or liquids have not been reported to date. The thickness profile and the associated dewetting dynamics in the entrapped air layer are investigated experimentally and theoretically using high-speed reflection interferometric imaging and linear stability analysis. We attribute the formation of multi-scale thickness perturbations, associated ruptures, and finger-like protrusions in the draining air film as a combined artifact of thin-film and Saffman–Taylor instabilities. The characteristic length scales depend on the air layer dimensions, the ratio of the liquid pool to droplet viscosity, and the air–water to air–oil surface tension.

I. INTRODUCTION

Drop impacts on liquid pools are ubiquitous in many industrial, biological, agricultural, and medical applications.[1–3] The droplet and the liquid pool deform prior to impact[4–6] due to the lubrication pressure of the entrapped air between the pool and the droplet [Fig. 1(a)]. The entrapped air layer dynamics beneath the droplet provide insights into various types of bubble formation mechanisms like Messler entrainment, bubble chandeliers, and hanging necklaces[7,8] [Fig. 1(b)]. Various research groups[9–11] pursue drop impact physics experimentally and theoretically due to its application in 3D printing, spray painting, and novel cooling technologies.[11–13] Air bubbles of various sizes that get entrapped during spray coating are detrimental to superior surface finish. On the other hand, air bubbles trapped by raindrops provide a mechanism of gaseous exchange between the atmosphere and natural water bodies that support a wide variety of aquatic life forms.[14]

Bubble entrapment mechanisms during various kinds of drop impacts on solids and liquids were studied by many groups.[14] The bubble entrapment mechanism for drop impact on pools is related to the *entrapped air layer dynamics* that form the central theme of our work. The outcome of the drop impact dynamics on solids and liquids depends on numerous parameters like fluid properties, impact velocity, atmospheric pressure, plate temperature, and droplet size, to name a few. The pool depth is also an essential parameter for impact on liquid pools. Hicks *et al.*[4,5] studied the effect of liquid pool height on air cushioning and splash dynamics for drop impact. Hicks and coworkers showed that a critical balance occurs when the pool depth is of the same order of magnitude as the horizontal extent of interactions between the pool and drop. The air layer dynamics do not depend on the pool height and pool base for a significant depth (deep pool limit). On the contrary, the air layer dynamics during drop impact on a solid surface can be thought of as a limiting case of drop impact on liquid pools with negligible depth compared to drop radius (shallow pool limit). The entrapped air layer dynamics lie between deep and shallow pool limits for all impact conditions. The rise in pressure deforms the droplet forming the *central dimple* prior to impact [Fig. 1(a)]. The lubrication pressure of the entrapped air is inversely proportional to the air layer thickness and, hence, increases as the droplet approaches the liquid pool. The effect of lubrication pressure decreases in the radial direction forming a thin air layer region surrounding the central air dimple, which we refer to as the *peripheral air disk* [Fig. 1(a)]. The air thickness near the dimple is relatively higher [$\mathcal{O}(10^1)$] than the peripheral air disk region. In general, the air disk curves radially upwards for impact on liquids.

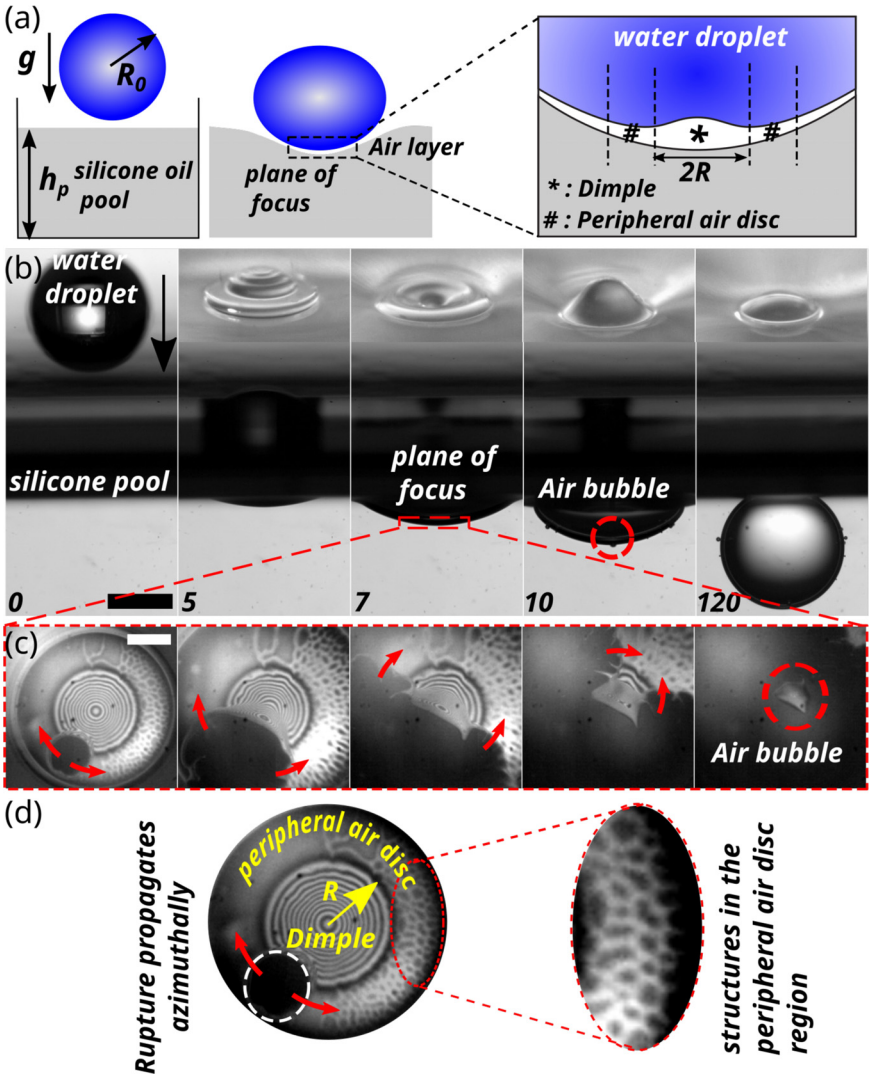

FIG. 1. Overview of the various physical processes beneath an impacting water droplet on silicone oil. (a) The schematic representation of the air layer between the impinging water droplet (blue color) and the silicone oil pool (gray color). g represents acceleration due to gravity, and R_0 represents the impinging droplet radius. The plane of focus marked by the dotted rectangle is shown as an expanded view on the right. Dimple and peripheral air disk are represented as $*$ and #, respectively. The dimple diameter is represented as $2R$. (b) Time series snapshots during the impact on silicone pool. The time-stamps are in milliseconds. The black scale bar represents 1 mm. Air bubbles (red dotted circle) can be observed at 10 ms and beyond. (c) High-speed reflection interferometric time-series images of the air layer beneath the impinging droplet. The air layer rupture propagates in the azimuthal direction (red arrows) and forms the air bubble (red dotted circle). The white scale bar represents 250 μm. (d) Magnified view of the air entrapped between the water droplet and the silicone pool. The air layer consists of two regions: the dimple of radius R and the peripheral air disk.

However, the curvature depends on the impact Weber number ($We = \rho_w V_0^2 R_0/\sigma$) and liquid pool properties like viscosity, where ρ_w is the density of the impinging droplet (water here), V_0 is the impact velocity, R_0 is the radius of the impinging droplet, and σ is the liquid–air surface tension. The high impact Weber number and low liquid pool viscosity result in significant air disk curvature.[15] However, with an impact on highly viscous liquid pool like silicone oil at a relatively small Weber number ($We < 15$), the curvature reduces significantly. Therefore, the peripheral air disk can be approximated as a flat region (a tangent plane approximation). Researchers have studied the central dimple extensively[15–17] in the context of impacts on liquids and solids. However, the nature of the peripheral air disk and its associated dewetting dynamics is relatively unknown.

In this study, we investigate the air layer dynamics in the central dimple and peripheral disk region for relatively low impact Weber number [$We \sim \mathcal{O}(10)$] on silicone oil pool of three different viscosities using experimental and theoretical scaling analysis. The entrapped air forms two distinct interfaces for drop impacts on immiscible liquids, i.e., top interface with the impacting droplet (water) and bottom interface with the liquid pool (silicone oil). The draining of the entrapped air due to the squeezing action of the impinging droplet can be formulated as a dewetting process. As the entrapped air layer thickness (h) in the disk region reduces to $h \sim 100$ nm, the air layer dewetting/draining dynamics are affected by molecular interaction potentials like van der Waals attraction and double-layer repulsion.[18] New fundamental length scales like spinodal structures[19] can exist in metastable state due to the balance of capillary and intermolecular forces. Such spinodal dewetting patterns were observed in condensed matter systems like thin polymers, liquid crystals, and liquid metal films.[20–24] However, dewetting patterns in gaseous media (air here) in drop impact studies are relatively unknown in the scientific community. We propose the topology observed in the peripheral air disk results as a combined effect of the thin-film/spinodal instability and the Saffman–Taylor instability. Saffman Taylor/viscous fingering are

formed at an unstable interface of differential viscosity where the less viscous fluid pushes a high viscous fluid. Viscous fingering has been intensively studied in the fluid dynamics community.[25–29] The mechanism of viscous fingering is dominantly observed in porous media and drainage processes. Finger-like structures near the vicinity of the central air dimple during drop impacts have not been reported to date. We have observed hydrodynamic structures in the dewetting peripheral air disk surrounding the central dimple that resembles the finger-like structures. We attribute the instability structures as a combined artifact of thin-film[18] and Saffman–Taylor instabilities.[25] The peripheral air disk thins out due to pressure-induced height fluctuations similar to the dewetting mechanism in thin polymer films.[20] This is because thin-film instability causes the interface to develop perturbations, which further act as a scaffolding for the Saffman–Taylor instability to form finger-like structures that propagate in the radial direction.

Figure 1(a) shows a schematic representation of the air layer entrapped between an impinging water droplet and a silicone oil pool. The pressure in the entrapped air layer increases as the droplet approaches the liquid pool. The increased pressure in the air layer results in a dimple formation. The entrapped air layer is divided into two connected regions, the central dimple (marked as $*$) and the peripheral air disk (marked as #). New topological structures were detected in the peripheral air disk region. Figure 1(b) depicts the impact event captured using high-speed shadowgraphy and perspective view imaging. The plane of focus of the reflection interferometry setup is marked with a dotted red rectangle. Figure 1(c) shows high-speed interferogram snapshots that reveal the hydrodynamic structures in the peripheral air disk. The azimuthal air layer ruptures and propagates (marked by a red arrow), forming the central air bubble (marked by a red dotted circle). Figure 1(d) shows the magnified view of the air disk where the dimple radius is represented as R. The lack of left–right symmetry in the air disk is due to slight asymmetry in the air layer entrapment during drop impact. Refer to Fig. S1 in the supplementary material text for an example of symmetric patterns observed throughout the peripheral air disk.

II. MATERIALS AND METHODS

A. Experimental setup

Figure 2(a) shows the schematic representation of the experimental setup. Figure 2(b) shows the photograph of the actual experimental set-up used. It consists of two high-speed cameras (Photron SA5), a pulse-diode laser source for interferometric illumination (Cavitar Cavilux smart UHS, 400 W power, $\lambda = 632$ nm), a white light source for shadowgraphy, interferometric optics (including a Navitar zoom lens, dichoric mirror, and beam splitter), a microscope objective (5×, 10×, and 20×), a liquid pool of silicone oil, and a syringe pump (New Era Pump Systems, NE-1010) for generating droplet of radius $R_0 \sim 1mm$. We used high-speed reflection interferometric imaging at 10 000–50 000 frames per second using a monochromatic diode laser source (632 nm). A spatial resolution of 1.5 μm per pixel was used to resolve the constructive and destructive interference patterns. We have explored the air layer dynamics at the low impact Weber number regime ($We \sim 10$) due to the dominant effect of the air cushion. The droplet was allowed to fall freely under gravity to achieve a particular impact Weber number. In this study, we focus on the effect of the liquid pool viscosity on the air layer dynamics at a constant impact Weber number of approximately ($We \sim 10$). Deionized water droplet of radius 1.1 mm was used as the impinging droplet, while silicone oil of three different kinematic viscosities of (5, 350, and 950 cSt) was used for the pool. The silicone pool height [refer to Fig. 1(a)] was maintained at approximately five times the droplet radius ($h_p \sim 5R_0$). We used high-speed interferograms to evaluate the air layer thickness profile. The images were acquired with Photron FastCam Viewer (software package 4.0.3.4.), and the raw images were processed using a combination of open-source tools like ImageJ[30] and python.[31] Sufficient number of experimental runs (150) were conducted on three different viscosity of silicon oils to ensure statistically significant datasets. Preprocessing of the raw images was performed using FFT Bandpass Filter[32] and CLAHE (Contrast Limited Adaptive Histogram Equalization).[33] The significant structures were filtered down to 40 pixels, and small structures up to 3 pixels were used for the FFT Bandpass Filter. For CLAHE, a block size of 127 pixels was used along

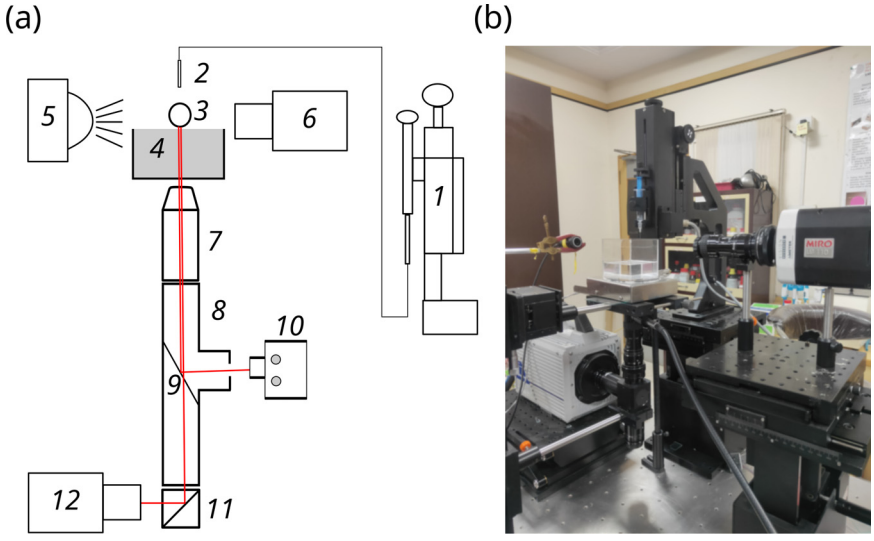

FIG. 2. (a) Schematic of the experimental setup. Various components of the setup are labeled by numeric values. 1, Syringe pump; 2, needle; 3, water droplet; 4, silicone oil liquid pool; 5, backlight source for shadowgraphy; 6, high-speed camera; 7, microscope objective; 8, zoom lens; 9, beam splitter; 10, laser source; 11, dichoric mirror. (b) Photograph showing the actual experimental set-up.

with histogram bins of 256 and a maximum slope of 3. The various kinematic parameters involved were then tracked, and the results were post-processed using Python.[31] The discrete raw data of the kinematic parameters were converted into a continuous probability density function (PDF) using kernel density estimate. The Gaussian kernel has been used for the kernel density estimate.

B. Evaluation of air layer thickness profile from interferograms

A monochromatic light beam from the diode source propagates through the microscope objective (20×) and travels toward the silicone oil-free surface. A part of the incident light gets reflected at the air–oil interface to register an intensity I_1; the transmitted light travels through the air layer between the droplet and pool, causing another reflection from the bottom surface of the impinging droplet that gives rise to intensity of I_2. Lights of intensity I_1 and I_2 (with a phase shift due to the additional optical path traveled) interfere and form a resultant intensity pattern I expressed in the form[34–36]

$$I(x_1, x_2) = I_1 + I_2 + 2\sqrt{I_1 I_2}\cos(\phi(x_1, x_2)), \tag{1}$$

where $\phi(x_1, x_2)$ is the phase shift. The interference patterns are captured using high-speed cameras. Sample interferograms are shown in Fig. 3. Here, x_1, x_2 represent the acquired two-dimensional image coordinates. The main feature of Eq. (1) is to quantify the fringe patterns depending on the variation of a cosine-modulated function. Hence, if the phase gradient is high, high-density fringes are observed. Similarly, a smaller phase gradient corresponds to low fringe density.

In this context, the developed fringe patterns during droplet impingement have been processed by employing the fast-frequency guided sequential demodulation (FFSD) method.[33,34,37,38] Fast-frequency guided algorithms are suitable for transient phenomena and consequent comprehensive extraction of the two-dimensional phase field of the complex fringe patterns. The gradient of phase distribution for the obtained fringe patterns has been estimated from the fast-frequency-guided sequential demodulation given as[37]

$$\phi(x_1, x_2) = \omega(x_1, x_2)e^{i\theta(x_1, x_2)}. \tag{2}$$

Here, $\omega(x_1, x_2)$ signifies the amplitude to determine the local frequencies precisely in the spatial domain through frequency-guided strategy, and θ denotes the angle of the complex number determined from the initial intensity variables. The obtained phase variables are constructed to be continuous and unwrapped. The height of the air layer profiles can be estimated for the preferred wavelength of the light source λ and refractive index n of the fluid medium as[39]

$$h(x_1, x_2) = \frac{\lambda}{2\pi n}\phi(x_1, x_2). \tag{3}$$

III. RESULTS

The air layer beneath the impacting droplet on a liquid pool consists of two distinct connected regions: a central dimple and the peripheral air disk [Figs. 3(a) and 3(b)]. The dimple radius R, height h_0, and the initial radial air velocity was observed to be the largest for impact on 5 cSt followed by 350 and 950 cSt. However, the peripheral air disk was the smallest for 5 cSt, followed by 350 and 950 cSt

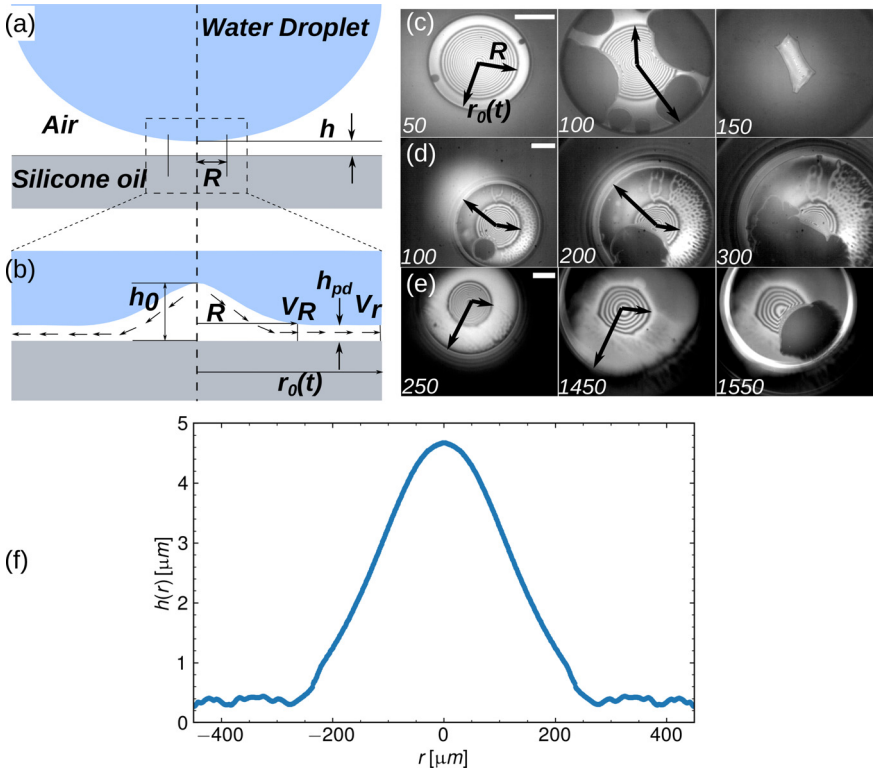

FIG. 3. (a) Schematic representation of the droplet impact phenomena on the liquid pool just prior to the formation of the central dimple. (b) Magnified view of the fully formed central dimple and the peripheral air disk. The relevant dimensions are annotated. h_0 denotes the dimple height, R represents the dimple radius, and h_{pd} represents the thickness of the peripheral air disk. High-speed reflection interferometric image sequence depicting peripheral air disk expansion. The scale bar in white represents 250 μm. The relative timestamps are in microseconds. The dimple radius is represented as R; expanding peripheral air disk radius is represented as $r_0(t)$. (c) High-speed interferometry snapshots during impact on 5 cSt silicone oil pool. (d) High-speed interferometry snapshots during impact on 350 cSt silicone oil pool. (e) High-speed interferometry snapshots during impact on 950 cSt silicone oil pool. (f) A typical air layer thickness profile computed from the experimental interferometric data using Eq. (3). The profile is plotted for impact on 350 cSt silicone oil at 900 μs. Multimedia views: https://doi.org/10.1063/5.0091584.1; https://doi.org/10.1063/5.0091584.2; https://doi.org/10.1063/5.0091584.3

[Figs. 3(c), 3(d), and 3(e) show the interferogram snapshots for impact on 5, 350, and 950 cSt silicone oil]. The peripheral air disk radius $r_0(t)$ dependence on time was found to be $t^{2/3}$ as a result of a small Capillary number ($Ca = \mu_a V_0/\sigma_{aw}$), where μ_a is the air viscosity, V_0 is the impact velocity, and σ_{aw} is the air–water surface tension. Further, the peripheral air disk thickness was one order smaller than the central air dimple thickness. The air disk on 5 cSt was highly unstable compared to 350 and 950 cSt resulting in very fast ruptures [compare the time scales of Figs. 3(c)–3(e)]. Figure 4(a) shows the region of focus for capturing the interference signals. Figure 4(b) shows the intensity map of the interference signals plotted as a 3D surface. Unique spinodal and finger-like structures in the peripheral air disk were observed for drop impact on 350 and 950 cSt at the impact Weber number of $We \sim \mathcal{O}(10)$ using high-speed reflection interferometric imaging [Figs. 4(b)–4(d)]. We propose that the structures in the peripheral air disk result due to the combined effect of thin-film/spinodal and Saffman–Taylor instabilities. Scaling and linear stability analysis was used to unearth the air layer dynamics and the related instabilities beneath the impacting droplet. The length scales of experimentally measured structures [Fig. 4(d)] conform to the most unstable wavelength of the thin film [$\lambda_{TF} \sim \mathcal{O}(14.72\,\mu\text{m})$] and Saffman–Taylor instabilities [$\lambda_{ST} \sim \mathcal{O}(13.89\,\mu\text{m})$]. [Refer to Fig. 3(c), Multimedia view, Fig. 3(d), Multimedia view, and Fig. 3(e), Multimedia view, for the high-speed interferograms visualizing the entrapped air layer dynamics for impact on 5, 350, and 950 cSt silicone oil, respectively.] Figure 3(f) shows a typical air layer thickness profile computed from the experimental interferometric data using Eq. (3). The profile is plotted for impact on 350 cSt silicone oil at 900 μs.

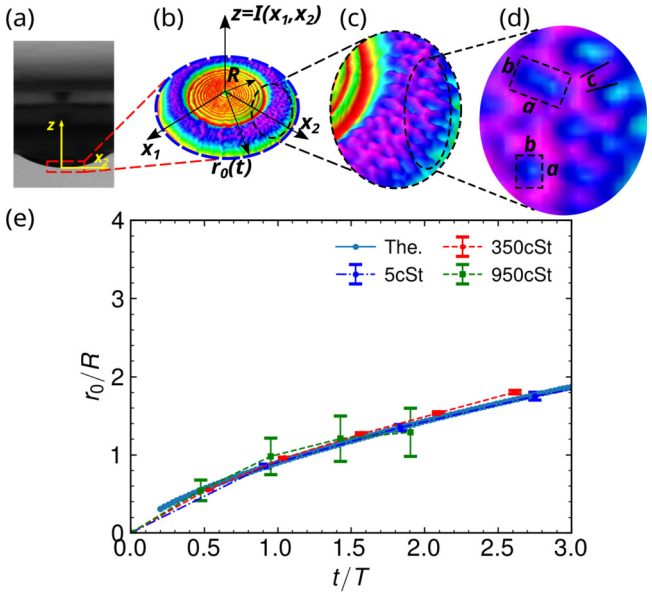

FIG. 4. (a) Region of focus for bottom view interferometric imaging shown as a dotted red rectangle. (b) 3D visualization of the reflection interferometric signal (False color). (c) Zoomed-in 3D view of the peripheral air disk region. (d) Relevant experimental length scales in the peripheral air disk region. *a*, *b* experimentally characterize the length scales over which the air thickness height changes. The finger-like structures observed at the advancing front of the peripheral air disk can be characterized experimentally using the finger width *c*. (e) Comparison of the experimental and theoretical air disk expansion characteristics (peripheral air disk radius r_0) for drop impact on 5, 350, and 950 cSt silicone oil. *R* denotes the dimple radius, and *T* denotes the time interval during which the dimple radius *R* becomes approximately constant.

IV. DISCUSSIONS

The droplet on approach toward the liquid pool displaces the air entrapped in a thin region [Fig. 1(a)]. Two distinct connected regions exist and characterize the air layer: the central dimple and the peripheral air disk surrounding the dimple. The air layer dynamics in both regions are presented in the following subsections (Secs. IV A and IV B) using scaling analysis.

A. Dynamics of the entrapped air layer (dimple region)

Figure 3(a) schematically represents the air layer as the droplet approaches the liquid pool. The impacting water droplet is shown in blue, the silicone oil pool in gray, and the entrapped air layer in white. A cylindrical control volume beneath the impacting droplet of radius R and height h was chosen for the subsequent analysis. Applying conservation of mass in the control volume assuming air to be in-compressible (low Mach number) and having a constant density, we have

$$V_0 \pi R^2 = V_R 2\pi R h, \tag{4}$$

where V_0 is the impact velocity, R is a radial length scale characterizing the air layer and represents the dimple radius, and V_R is the air velocity at the edge of the dimple at the initial phase of expansion. The radial air velocity V_R at a radial distance R from the center could be expressed in terms of the impact velocity V_0, length scales h and R as

$$V_R = \frac{V_0 R}{2h}, \tag{5}$$

where the scale of h is still unknown. As the droplet approaches, the pressure in the air layer increases resulting in the formation of the dimple as shown in Fig. 3(b). The thin entrapped air region can be modeled using the Stokes equation to first-order accuracy as was shown by Hicks *et al.*[4]

$$\mu_a \nabla^2 \boldsymbol{V} \sim \nabla p_a. \tag{6}$$

As the air layer thickness is relatively small compared to the droplet radius, lubrication approximation (ref) is valid for the entrapped air layer. The dominant forces in the entrapped air layer region are the viscous forces and the pressure gradient. The radial component of Eq. (6) under the lubrication approximation can be written as

$$\frac{\partial^2 V_r}{\partial z^2} \sim \frac{1}{\mu_a}\frac{\partial p_a}{\partial r}, \tag{7}$$

where the V_r denotes the radial air velocity, z represents the axial coordinate orthogonal to the radial direction, p_a represents the air pressure in the entrapped air layer, μ_a represents the air viscosity, and r denotes the radial coordinate. Rewriting Eq. (7) in terms of the dominant scales ($V_r \sim V_R$, $z \sim h$, $p_a \sim \Delta p_a$), we have

$$\frac{\Delta p_a}{R} \sim \frac{\mu_a V_R}{h^2}. \tag{8}$$

Using the scale of V_R from Eq. (5) in Eq. (8) and solving for the scale of Δp_a, we have

$$\Delta p_a \sim \frac{\mu_a V_0 R^2}{2h^3}. \tag{9}$$

The pressure in the thin air film region scales as $\Delta p_a \sim h^{-3}$. Therefore, as the air film thickness decreases, the pressure increases. For a certain critical height $h = h_*$, the air pressure becomes comparable to the capillary pressure ($2\sigma_{aw}/R_0$) at the air–water interface that leads to the formation of an air dimple. Therefore, at the critical air layer thickness, the equivalence of pressure scales leads to

$$\frac{\mu_a V_0 R^2}{2h_*^3} \sim \frac{2\sigma_{aw}}{R_0}. \tag{10}$$

From Eq. (10), the scale of h_* can be evaluated as

$$h_* \sim \left[\frac{\mu_a V_0 R^2 R_0}{4\sigma_{aw}}\right]^{1/3}, \tag{11}$$

where σ_{aw} is the air water surface tension. Using the definition of capillary number $Ca = \mu_a V_0/\sigma_{aw}$, Eq. (11) can be written as

$$h_* \sim \left[\frac{CaR^2 R_0}{4}\right]^{1/3}. \tag{12}$$

Equation (12) implies the existence of a critical air layer thickness at which the pressure rise in the air layer surpasses the capillary pressure of the approaching water droplet causing a dimple to form in the center of the droplet. Using the numerical values of impact velocity $V_0 \sim \mathcal{O}(0.5\,\mathrm{m/s})$, air viscosity $\mu_a \sim \mathcal{O}(1.81 \times 10^{-5}\,\mathrm{kg/ms})$, air–water surface tension $\sigma_{aw} \sim \mathcal{O}(0.072\,\mathrm{N/m})$, dimple radius $R \sim \mathcal{O}(200 \times 10^{-6}\,\mathrm{m})$, and droplet radius of $R_0 \sim \mathcal{O}(1.1 \times 10^{-3}\,\mathrm{m})$, the critical thickness is $h_* \sim \mathcal{O}(2.17 \times 10^{-6}\,\mathrm{m})$. The Capillary number for $V_0 \sim \mathcal{O}(0.5\,\mathrm{m/s})$ is $Ca \sim \mathcal{O}(1.26 \times 10^{-4})$ signifying surface tension effects are dominant compared to viscous effects in the entrapped air layer. The dimple height at the center h_0 will be of the same order of magnitude as h_*, however, $h_0 \gtrsim h_*$, due to the formation of the central air dimple. Using the value of h_* from Eq. (12) in Eq. (5), the initial radial air velocity scale at the edge of the central dimple ($r = R$) becomes

$$V_R \sim \frac{V_0 R}{2}\left[\frac{\mu_a V_0 R^2 R_0}{4\sigma_{aw}}\right]^{-1/3}. \tag{13}$$

Rearranging the above equations and non-dimensionalizing with respect to the impact velocity V_0, we have

$$\frac{V_R}{V_0} \sim \left[\frac{1}{2Ca}\frac{R}{R_0}\right]^{1/3}. \tag{14}$$

The initial radial air velocity at the edge of the central dimple is $V_R \sim \mathcal{O}(4.77\,\mathrm{m/s})$, and the order of magnitude conforms with the experimental peripheral air disk velocity. The experimentally measured initial peripheral air disk velocity for 5, 350, and 950 cSt is of the order of 5.32, 2.52, and 1.71 m/s, respectively.

B. Dynamics of the entrapped air layer (expansion of the peripheral air disk)

As the peripheral air disk radius becomes larger than the dimple radius [$r(t) > R$], the air disk expands due to the effect of surface tension forces at the top (air–water) and bottom (air–silicone) interface. This is due to a very low value of Capillary number [$Ca \sim \mathcal{O}(1.26 \times 10^{-4})$] signifying surface tension effects are stronger than viscous effects. Newton's second law applied to the expanding air disk gives

$$\rho_a \frac{d^2 r_0}{dt^2} \sim \frac{2(\sigma_{aw} + \sigma_{as})}{L}\frac{d^2 h}{dr^2}, \tag{15}$$

where ρ_a is the air density, σ_{aw} is the air–water surface tension, σ_{as} is the air silicone oil surface tension, h represents the air layer height profile as a function of radial coordinate r, and L is a characteristic length scale orthogonal to the radial coordinate and related to the air layer geometry. The left-hand side of Eq. (15) represents the inertial terms per unit volume, and the right-hand side represents the surface tension forces along with the air–water and air–silicone interface. Rewriting the scaling form of Eq. (15) using the dominant scales ($r \sim r_0$, $L \sim h \sim h_{pd}$), where h_{pd} is the thickness of the peripheral air disk, we have

$$\frac{\rho_a r_0}{t^2} \sim \frac{2(\sigma_{aw} + \sigma_{as})h_{pd}}{h_{pd} r_0^2}. \tag{16}$$

Rearranging Eq. (16) and solving for the scale of r_0, we have

$$r_0 \sim \left(\frac{2(\sigma_{aw} + \sigma_{as})}{\rho_a}\right)^{1/3} t^{2/3}. \tag{17}$$

Non-dimensionalizing Eq. (17) with respect to the dimple radius R gives us

$$\frac{r_0}{R} \sim \left(\frac{2(\sigma_{aw} + \sigma_{as})T^2}{\rho_a R^3}\right)^{1/3}\left(\frac{t}{T}\right)^{2/3} = \Gamma\left(\frac{t}{T}\right)^{2/3}, \tag{18}$$

where R is the dimple radius, T is the timescale at which the peripheral air disk radius becomes constant, and

$$\Gamma = \left(\frac{2(\sigma_{aw} + \sigma_{as})T^2}{\rho_a R^3}\right)^{1/3}. \tag{19}$$

Figure 4(e) shows the comparison of the experimental peripheral air disk radius evolution with the theoretical scaling predicted by Eq. (18). The experimental value of $\Gamma \sim \mathcal{O}(0.9)$, whereas the theoretical scale of Γ for 5, 350, and 950 cSt are 2.81, 4.95, and 7.44, respectively. It can be inferred from Fig. 4(e) that the experimental scale conforms with the theoretical scale predicted by Eq. (18) and by the fact that the numerical value of $\Gamma \sim \mathcal{O}(1)$ experimentally as well as theoretically.

C. Structures in the peripheral air disk region

1. Physical mechanism for structure formation in the peripheral air disk

The peripheral air disk expands in the radial direction according to Eq. (18). As was discussed in Secs. I and III, unique hydrodynamic structures were observed in the peripheral air disk [Fig. 4(d)]. To characterize the structures present in the peripheral air disk, the spatial intensity distribution of the interferograms was decomposed into orthogonal spatial modes using SVD (singular value decomposition) based proper

orthogonal decomposition (POD) method.[40,41] The POD was performed to identify and distinguish various length scales present in the disk region. We found that the structures in the peripheral air disk are layered in a very thin region of the order of the dimension of the fingers. Figure 5(a) shows the input image to the POD algorithm. The input image corresponds to the peripheral air disk region surrounding the central air dimple. The first three dominant modes are shown in Figs. 5(b), 5(c), and 5(d), respectively. The POD modes are rank-ordered, with the first mode being the most dominant. Figure 5(e) shows the percentage energy distribution in various modes. The energies of individual modes were evaluated from the singular values. The first three modes mimic the essential length scales and their corresponding distributions

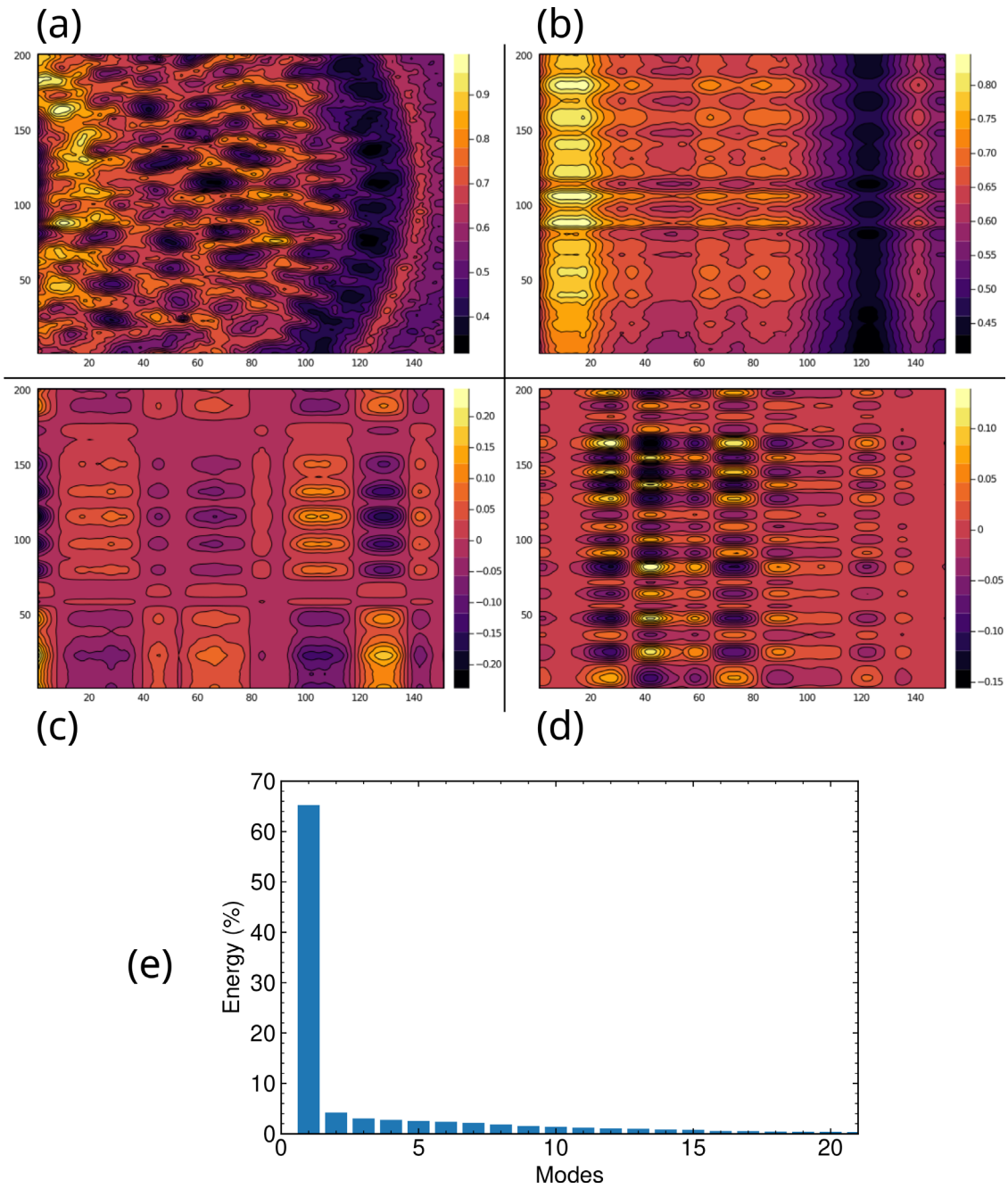

FIG. 5. SVD-based Proper orthogonal decomposition (POD) modes[40] of the peripheral air disk region computed using singular value decomposition method. (a) Input image used for extracting the proper orthogonal decomposition modes. (b) POD mode 1. (c) POD mode 2. (d) POD mode 3. (e) Percentage energy of various POD modes evaluated based on the singular values of the input image.

(approximately 75% of the total energy). As it can be inferred from the various decomposed modes, the peripheral air disk has intensity fluctuations that have both radial and azimuthal components. As the air layer drains out, the thickness in the peripheral air disk reduces to less than one micrometer. At these small scales, peripheral air disk thickness h_{pd} exists as a balance between the pressure in the air layer and the disjoining pressure. The disjoining pressure scales as A/h^3, where A is the Hamackers constant. The pressure in the air layer scales as σ_{aw}/R_0 as discussed in Sec. IV A. Therefore, the balance of disjoining and the air pressure leads to

$$\frac{A}{h_{pd}^3} \sim \frac{\sigma_{aw}}{R_0}. \tag{20}$$

Solving for the scale of h_{pd}, we have

$$h_{pd} \sim \left[\frac{AR_0}{\sigma_{aw}}\right]^{1/3}. \tag{21}$$

Using the value of $A \sim \mathcal{O}(5 \times 10^{-19})$,[42] the peripheral air disk thickness scale predicted from Eq. (21) is $h_{pd} \sim \mathcal{O}(1.96 \times 10^{-7}\ \text{m})$ which agrees on an order of magnitude level with the experimental measured value of $\mathcal{O}(3.3 \times 10^{-7}\ \text{m})$, $\mathcal{O}(3.8 \times 10^{-7}\ \text{m})$, and $\mathcal{O}(4.1 \times 10^{-7}\ \text{m})$ for impact on 950, 350, and 5 cSt, respectively.

Figure 6 depicts the schematic representation showing the structure formation mechanism in the peripheral air disk. The peripheral air disk thickness is smaller than the central dimple thickness by an order of magnitude, i.e., $h_{pd}/h_0 \sim \mathcal{O}(10^{-1})$ [by comparing the order of magnitude of Eq. (21) and Eq. (12)]. The air layer thickness is the characteristic length scale for the viscous effects. Based on the air layer thickness, the entrapped air's Reynolds number (Re_a) is small. $Re_a \sim \mathcal{O}(1)$ in the dimple region, and $Re_a \sim \mathcal{O}(10^{-1})$ in the peripheral air disk region. The low value of the Reynolds number revalidates the existence of the Stokesian flow in the air layer where viscous stresses balance the pressure gradient as we have discussed in Eq. (6). As the entrapped air drains out, small perturbations develop and trigger an instability [Fig. 6(a)]. The waves are present in both the top and the bottom interface of the air layer; however, the air–silicone interface becomes more unstable due to the lower value of surface tension compared to air–water interface. Figure 6(a) depicts the initial fluctuation in the air layer due to thin-film instability. The fluctuations form an unstable interface where finger-like structures are formed and grow radially due to the Saffman–Taylor instability [Fig. 6(b)]. Figure 6(c) shows a cross-sectional view from the bottom in the plane P–P. The finger-like structures are shown in white and the silicone oil liquid pool in gray. Figure 6(d) depicts a contour plot of the interferometric data rescaled from the intensity range of [0,255] to [0,1]. The patterns formed resemble finger-like structures [compare qualitatively with Fig. 6(c)] caused due to the Saffman–Taylor instability. Figure 6(e) shows the raw experimental interference data used as an input to generate the contour intensity map of Fig. 6(d). The radial air layer thickness profile $h(r)$ obtained from the interference data is plotted for different pool viscosities for the same impact Weber number ($We \sim 10$) in Fig. 7(a) at 100, 450, 900 μs for 5, 350, and 950 cSt, respectively. Drop impact on 5 cSt has the highest air layer thickness followed by 350 and 950 cSt. The thickness profile shows detectable perturbations for 350 and 950 cSt in the peripheral air disk region (225 μm $< r <$ 450 μm); however, negligible perturbations were observed for

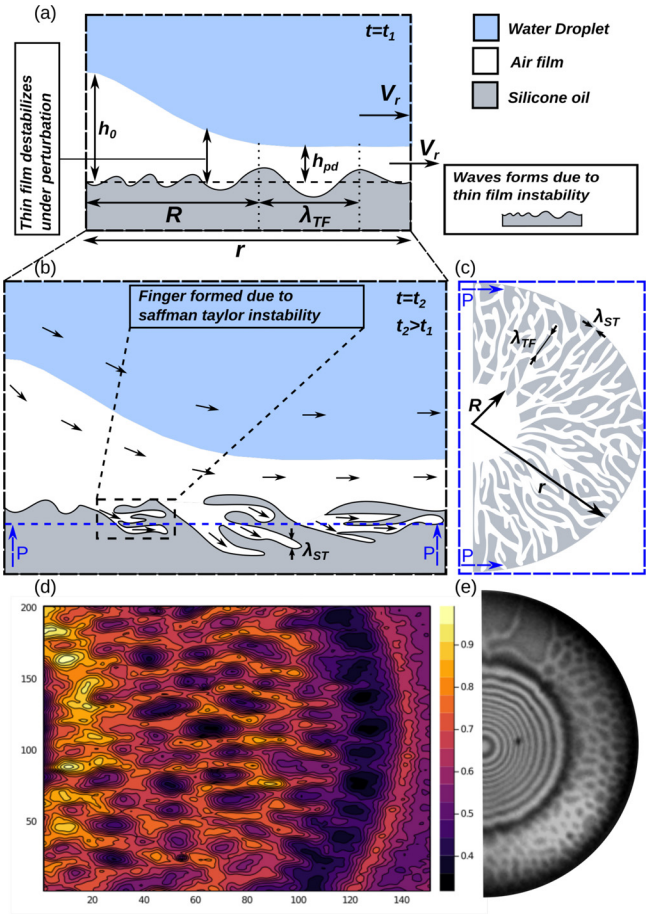

FIG. 6. Schematic representation depicting the mechanism of structure formation in the peripheral air disk region. (a) Schematic depicting thin-film instability and associated length scale fluctuations. (b) Schematic depicting the mechanism of the Saffman–Taylor instability leading to viscous fingering. (c) PP Cross-sectional view of radial air expansion causing finger-like structures to form and propagate as a fractal-like structures in the radial direction. (d) Experimental data depicting patterns in the peripheral air disk region. The patterns resemble finger-like structures formed due to the Saffman–Taylor instability. The plot represents contour map of the intensity data rescaled from the intensity range of [0, 255] to [0,1]. (e) Raw interference data used as input to generate the contour intensity map of Fig. 6(d).

5 cSt [Fig. 7(b)]. The perturbations observed in 350 cSt were more prominent (larger in amplitude) than in 950 cSt. We observe [Figs. 3 and 7(b)] that the peripheral air disk width is largest for 950 cSt, followed by 350 and 5 cSt, respectively. Further, we also observe that the timescale for air disk to rupture is largest for 950 cSt followed by 350 and 5 cSt (Fig. 3). The air layer for 950 cSt is comparatively more stable compared to 350 and 5 cSt. The characteristic length scales [Figs. 7(a) and 7(b)] relevant to the dynamics is the air layer thickness in the dimple region ($h_0 \sim$ 4–6 μm) and the peripheral air disk region ($h \sim$ 0.3–0.4 μm). The distinct air layer dynamics and dewetting characteristics observed are based on the implications of thin-film/spinodal and Saffman–Taylor stability characteristics in the peripheral disk region discussed in Secs. IV C 2 and IV C 3.

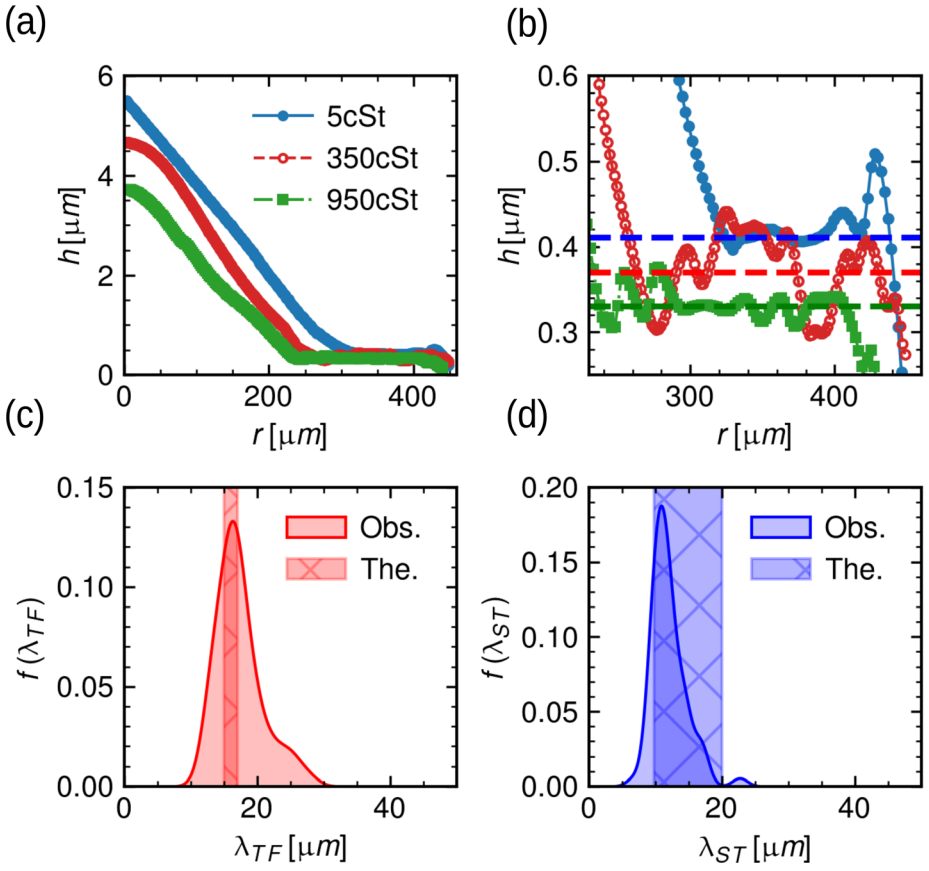

FIG. 7. (a) Air layer thickness profile $h(r)$ plotted as a function of radial distance for three different liquid pool viscosities plotted at 100, 450, 900 μs for 5, 350, and 950 cSt, respectively. (b) Air layer thickness profile in the peripheral air disk region. (c) The probability density function of the experimental length scales observed in the peripheral air disk region for 350 cSt compared with the theoretical wavelength estimated from the thin-film instability analysis. (d) Probability density function of the finger width c observed in the peripheral air disk region for 350 cSt compared with the theoretical estimates of the most dominant wavelength from the Saffman–Taylor instability theory.

2. Thin film/spinodal instability

The squeezing of the entrapped air continues as the droplet sinks in the pool. As the thickness becomes smaller than a micrometer ($h < 1\ \mu$m), Van der Walls force and double-layer interaction become comparable to capillary force, and hence, new length scales can exist in metastable state due to the balance of intermolecular and capillary forces[18,42] before rupture initiates. Following the reasoning given by Vrij,[18] the most dominant characteristic length scale due to intermolecular and capillary interaction for spinodal instability is given by λ_{TF}

$$\lambda_{TF} \sim h^2 \left(\frac{\sigma_{aw}}{A}\right)^{1/2}, \tag{22}$$

where h is the air layer thickness in the peripheral air disk and A is the Hamaker constant. Using $h = h_{pd}$ from Eq. (21) in (22), we have

$$\lambda_{TF} \sim \left[\frac{AR_0}{\sigma_{aw}}\right]^{2/3} \left[\frac{\sigma_{aw}}{A}\right]^{1/2} = \left[\frac{AR_0^4}{\sigma_{aw}}\right]^{1/6}. \tag{23}$$

The experimental probability density function (PDF) of the length scales in the peripheral air disk region {given by the arithmetic mean of a, b [Fig. 4(d)] of 63 measurements} is plotted in Fig. 7(c) (marked as Obs.) using kernel density estimate.[43] The experimental peak is approximately at 17 μm with a standard deviation of 3 μm which coincides remarkably to the scale predicted by Eq. (23). λ_{TF} calculated through Eq. (23) using $A \sim \mathcal{O}(5 \times 10^{-19}\ \text{J})$, $R_0 \sim \mathcal{O}(1.1 \times 10^{-3}\ \text{mm})$ gives $\lambda_{TF} \sim 14.72\ \mu$m. Below a certain critical thickness, $\lambda_{TF} \sim h^2$, which indicates that small value of thickness corresponds to small λ_{TF}. This trend is consistent with our observations for 350 and 950 cSt. The spread of the PDF in Fig. 7(c) is due to the multimodal nature of thin film instability generated due to height fluctuations.

3. The Saffman–Taylor Instability

The Saffman–Taylor instability, also known as viscous fingering, forms at the interface of differential viscosity and can occur in geometries without rigid walls.[44] Generally, instability occurs in porous media and Hele–Shaw configuration. In this work, we study drop impacts on the immiscible liquid pool. The droplet and the liquid pool deform prior to impact[4–6] due to the rise of lubrication pressure of the entrapped air between the pool and the droplet. The air entrapped forms a dimple surrounded by a peripheral air disk as the lubrication pressure becomes comparable and exceeds the capillary pressure of the impacting droplet. The entrapped air flows between two interfaces (the top is an air–water interface, and the bottom is an air–oil interface) as the droplet spreads/penetrates the impacting medium. The maximum air layer thickness (gap between the two interfaces) occurs at the dimple center [$h_0 \sim \mathcal{O}(5 \times 10^{-6}\ \text{m})$], and the peripheral air

disk thickness scale is $h_{pd} \sim \mathcal{O}(10^{-7}\,\mathrm{m})$. Compared to the radius of the peripheral air disk $r_0 \sim \mathcal{O}(250 \times 10^{-6}\,\mathrm{m})$, the air layer is entrapped in a very thin region, and a Hele–Shaw flow can approximate the fluid dynamics between the interfaces. The interface between two different viscosity fluids is unstable when a less viscous fluid (air here) displaces a more viscous (silicone oil here) fluid. However, the interface is stable in a contrasting situation where a more viscous fluid displaces a less viscous fluid. The governing dynamics of the Saffman–Taylor instability occur due to a balance of the viscous term and pressure gradient term in the Navier–Stokes equation. The balance between pressure and viscous forces occurs within a timescale characterized by the boundary layer growth timescale ($t_b \sim h^2/\nu_a$), where h is the air layer thickness and ν_a is the kinematic viscosity of air. For $h \sim h_0$, $t_b \sim 1.69\,\mu$s, the Saffman–Taylor instability occurs very fast within 1.69 μs in comparison to the peripheral disk expansion timescale of 100 μs, i.e., almost two orders of magnitude faster. The peripheral air disk thickness is one order smaller than the central dimple thickness ($h_0 \sim 10h_{pd}$), and the timescale required for the balance between viscous and pressure forces is of the order of nanoseconds [$t_b \sim \mathcal{O}(10^{-9}\,\mathrm{s})$]. Based on the above scales for t_b, we observe that the Saffman–Taylor instability in the entrapped air region can occur at a timescale faster than the peripheral air disk expansion timescale. The essential condition for finger-like structures to grow and propagate is that the unstable interface should have a velocity in a direction perpendicular to the interface relative to a particular fluid. The Saffman–Taylor instability for the experimental configuration studied originates from small height fluctuations in the air layer thickness profile (due to radial drainage of air) that acts as a scaffolding for the Saffman–Taylor instability to form unstable finger-like structures at the interface, which propagates in the radial direction. The initial air entrapped is not static but travels radially outwards and has a velocity perpendicular to the air–oil interface. The slight fluctuation in the thickness profile causes viscous fingering to initiate and travel radially outwards, forming finger-like structures observed experimentally. The interface of differential viscosity becomes unstable when a less viscous fluid (air here) displaces a high viscous fluid (silicone oil). The most dominant unstable wavelength due to the Saffman–Taylor instability in a radial Hele–Shaw configuration is given by[44]

$$\lambda_{ST} = 2\sqrt{3}\pi r\left(\frac{Qr}{2\pi M\sigma_{as}} + 1\right)^{-1/2}, \tag{24}$$

where r is a radial coordinate, Q is the volume flow rate of air per unit depth, M is the mobility of the air through the viscous silicone oil pool, and σ_{as} is the air–silicone oil surface tension. The volume flow rate through the peripheral air disk becomes

$$Qh_{pd} = V2\pi r h_{pd}. \tag{25}$$

On simplification, Eq. (25) becomes

$$Q = V2\pi r, \tag{26}$$

where V is the velocity at the interface of air silicone oil forming the fingers. The mobility of air through silicone oil is given as[44]

$$M = \frac{h_{pd}^2}{12\mu_s}. \tag{27}$$

Incorporating Eqs. (26) and (27) in (24), the most dominant Saffman–Taylor wavelength scale can be written as

$$\lambda_{ST} = 2\sqrt{3}\pi r\left(\frac{12\mu_s r^2 V}{\sigma_{as}h_{pd}^2} + 1\right)^{-1/2}, \tag{28}$$

where V is the radial velocity of the air layer across the silicone oil interface. The radial air velocity scale V is given as[44]

$$V = M\nabla p \sim \frac{h_{pd}^2\sigma_{aw}}{12\mu_a R_0 r}. \tag{29}$$

Substituting the scale of V from Eq. (29) in Eq. (28), we have

$$\lambda_{ST} \sim 2\sqrt{3}\pi r\left(\frac{\mu_s}{\mu_a}\frac{\sigma_{aw}}{\sigma_{as}}\frac{r}{R_0} + 1\right)^{-1/2}. \tag{30}$$

The experimental probability density function (PDF) of finger width c calculated using kernel density estimate[43] for 67 measurements is shown in Fig. 7(d) (marked as Obs.). The peak of the experimental PDF is ($c \sim 12\,\mu$m) with a standard deviation of 3 μm lies within the theoretical limits (marked as The.) ($\lambda_{ST} \sim 9$–$20\,\mu$m) predicted by the Saffman–Taylor instability theory.[25] The theoretical scaling for the finger width was calculated using Eq. (30) using a range of $50\,\mu\mathrm{m} < r < 200\,\mu\mathrm{m}$, and it conforms with the experimental range. Figure 7(d) shows that the experimental PDF distribution has a range from 7 to 23 μm. The distribution is multimodal in nature due to the dependence of λ_{ST} on the radial coordinate r.

Non-dimensionalizing Eq. (30) based on the dimple radius R, we have

$$\frac{\lambda_{ST}}{R} \sim 2\sqrt{3}\pi\left(\frac{\mu_s}{\mu_a}\frac{\sigma_{aw}}{\sigma_{as}}\frac{R}{R_0} + 1\right)^{-1/2}. \tag{31}$$

Theoretically, λ_{ST} depends on the viscosity ratio, surface tension ratio, and radial coordinate [Eqs. (30) and (31)]. Figure 8 depicts the dependence of the dimensionless Saffman–Taylor length scale λ_{ST}/R

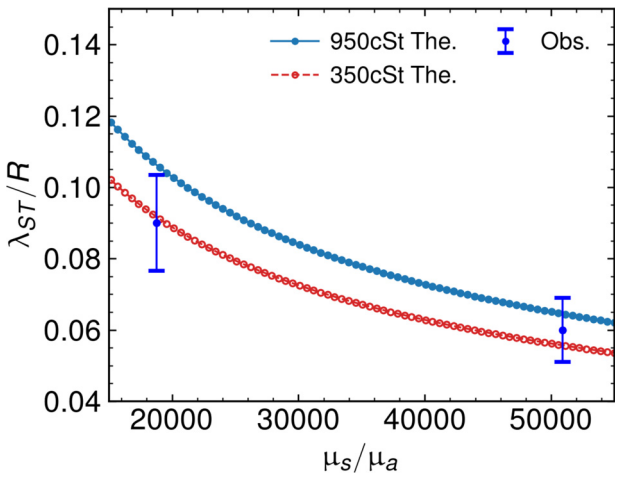

FIG. 8. Experimental and theoretical comparison depicting the dependence of the Saffman–Taylor wavelength [λ_{ST} as a function of viscosity ratio (μ_s/μ_a)] for 350 and 950 cSt.

on the viscosity ratio (μ_s/μ_a). The characteristic length scale has an inverse dependence on the viscosity ratio, indicating that as the viscosity ratio reduces, the length scale increases, which is consistent for our cases (Figs. 3 and 7). The experimental observation conforms with the theoretical scaling predicted by Eq. (30) on an order of magnitude sense. The two plotted experimental points represent the mean value of 67, 50 data points with a maximum standard deviation of 5% and 3% for 350 and 950 cSt. The azimuthal and the radial length scales are approximately of the same order of magnitude [Figs. 7(c) and 7(d)]. This is due to the fact that the thin-film instability causes the air–silicone oil interface to develop perturbations, which further acts as a scaffolding for the Saffman–Taylor instability to form finger-like structures that grows and propagates as fractal-like structure in the radial direction.

V. CONCLUSION

In conclusion, we observed that the central air dimple thickness h_0 and the peripheral air disk expansion were fastest for 5 cSt followed by 350 and 950 cSt, respectively. On the contrary, the air disk for 950 cSt is the most stable, followed by 350 and 5 cSt indicating largest rupture timescale for 950 cSt. Furthermore, it was also shown that the peripheral air disk radius r_0 grows as $t^{2/3}$ due to very small capillary number [$Ca \sim \mathcal{O}(10^{-4})$]. Unique hydrodynamic structures in the peripheral air disk during drop impact on the immiscible liquid pool of 350 and 950 cSt at the low impact Weber number ($We \sim 10$) was observed. Morphology of the structures shows that the characteristic wavelength observed aligns with the predictions of the thin-film/spinodal [$\lambda_{TF} \sim \mathcal{O}(14.72\,\mu\text{m})$] and Saffman–Taylor instability $\lambda_{ST} \sim \mathcal{O}(13.89\,\mu\text{m})$ length scales.

SUPPLEMENTARY MATERIAL

See the supplementary material for Fig. S1: an interferometric snapshot depicting a uniform pattern throughout the peripheral air disk on 350 cSt silicone oil pool. Data SD1: A zip file is provided carrying the data used in the analysis.

ACKNOWLEDGMENTS

The authors are thankful for the funding received from the Defence Research and Development Organization (DRDO) Chair Professorship.

AUTHOR DECLARATIONS

Conflict of Interest

The authors declare no conflict of interest.

Author Contributions

D.R. and S.M. proposed the problem statement. D.R., S.M., and S.S.R. performed the experiments and data analysis. D.R. and S.B. carried out the theoretical analysis and wrote the paper. S.B. supervised the project.

DATA AVAILABILITY

The data that support the findings of this study are available within the article and its supplementary material.

REFERENCES

[1]E. Castillo-Orozco, A. Davanlou, P. K. Choudhury, and R. Kumar, "Droplet impact on deep liquid pools: Rayleigh jet to formation of secondary droplets," Phys. Rev. E **92**, 053022 (2015).
[2]Q. Ye and J. Domnick, "Analysis of droplet impingement of different atomizers used in spray coating processes," J. Coat. Technol. Res. **14**, 467–476 (2017).
[3]M. Epstein and H. Fauske, "Applications of the turbulent entrainment assumption to immiscible gas-liquid and liquid-liquid systems," Chem. Eng. Res. Des. **79**, 453–462 (2001).
[4]P. D. Hicks and R. Purvis, "Air cushioning and bubble entrapment in three-dimensional droplet impacts," J. Fluid Mech. **649**, 135–163 (2010).
[5]P. D. Hicks and R. Purvis, "Air cushioning in droplet impacts with liquid layers and other droplets," Phys. Fluids **23**, 062104 (2011).
[6]S. Thoroddsen, T. Etoh, and K. Takehara, "Air entrapment under an impacting drop," J. Fluid Mech. **478**, 125–134 (2003).
[7]J. R. Saylor and G. D. Bounds, "Experimental study of the role of the Weber and capillary numbers on Mesler entrainment," AIChE J. **58**, 3841–3851 (2012).
[8]S. T. Thoroddsen, M.-J. Thoraval, K. Takehara, and T. Etoh, "Micro-bubble morphologies following drop impacts onto a pool surface," J. Fluid Mech. **708**, 469–479 (2012).
[9]J. de Ruiter, F. Mugele, and D. van den Ende, "Air cushioning in droplet impact. I. Dynamics of thin films studied by dual wavelength reflection interference microscopy," Phys. Fluids **27**, 012104 (2015).
[10]J. de Ruiter, D. van den Ende, and F. Mugele, "Air cushioning in droplet impact. II. Experimental characterization of the air film evolution," Phys. Fluids **27**, 012105 (2015).
[11]C. Josserand and S. T. Thoroddsen, "Drop impact on a solid surface," Annu. Rev. Fluid Mech. **48**, 365–391 (2016).
[12]S. D. Aziz and S. Chandra, "Impact, recoil and splashing of molten metal droplets," Int. J. Heat Mass Transfer **43**, 2841–2857 (2000).
[13]Y. T. Aksoy, Y. Zhu, P. Eneren, E. Koos, and M. R. Vetrano, "The impact of nanofluids on droplet/spray cooling of a heated surface: A critical review," Energies **14**, 80 (2020).
[14]D. Woolf, I. Leifer, P. Nightingale, T. Rhee, P. Bowyer, G. Caulliez, G. De Leeuw, S. E. Larsen, M. Liddicoat, J. Baker *et al.*, "Modelling of bubble-mediated gas transfer: Fundamental principles and a laboratory test," J. Mar. Syst. **66**, 71–91 (2007).
[15]M. H. Hendrix, W. Bouwhuis, D. van der Meer, D. Lohse, and J. H. Snoeijer, "Universal mechanism for air entrainment during liquid impact," J. Fluid Mech. **789**, 708–725 (2016).
[16]R. C. van der Veen, T. Tran, D. Lohse, and C. Sun, "Direct measurements of air layer profiles under impacting droplets using high-speed color interferometry," Phys. Rev. E **85**, 026315 (2012).
[17]W. Bouwhuis, R. C. van der Veen, T. Tran, D. L. Keij, K. G. Winkels, I. R. Peters, D. van der Meer, C. Sun, J. H. Snoeijer, and D. Lohse, "Maximal air bubble entrainment at liquid-drop impact," Phys. Rev. Lett. **109**, 264501 (2012).
[18]A. Vrij, "Possible mechanism for the spontaneous rupture of thin, free liquid films," Discuss. Faraday Soc. **42**, 23–33 (1966).
[19]A. Pereira, P. Trevelyan, U. Thiele, and S. Kalliadasis, "Dynamics of a horizontal thin liquid film in the presence of reactive surfactants," Phys. Fluids **19**, 112102 (2007).
[20]R. Konnur, K. Kargupta, and A. Sharma, "Instability and morphology of thin liquid films on chemically heterogeneous substrates," Phys. Rev. Lett. **84**, 931 (2000).
[21]W. W. Zhang and J. R. Lister, "Similarity solutions for van der Waals rupture of a thin film on a solid substrate," Phys. Fluids **11**, 2454–2462 (1999).
[22]R. Xie, A. Karim, J. F. Douglas, C. C. Han, and R. A. Weiss, "Spinodal dewetting of thin polymer films," Phys. Rev. Lett. **81**, 1251 (1998).
[23]J. Bischof, D. Scherer, S. Herminghaus, and P. Leiderer, "Dewetting modes of thin metallic films: Nucleation of holes and spinodal dewetting," Phys. Rev. Lett. **77**, 1536 (1996).
[24]U. Thiele, M. G. Velarde, and K. Neuffer, "Dewetting: Film rupture by nucleation in the spinodal regime," Phys. Rev. Lett. **87**, 016104 (2001).

[25]P. G. Saffman and G. I. Taylor, "The penetration of a fluid into a porous medium or Hele-Shaw cell containing a more viscous liquid," Proc. R. Soc. London, Ser. A **245**, 312–329 (1958).
[26]P. Tabeling, G. Zocchi, and A. Libchaber, "An experimental study of the Saffman-Taylor instability," J. Fluid Mech. **177**, 67–82 (1987).
[27]H. Thome, M. Rabaud, V. Hakim, and Y. Couder, "The Saffman–Taylor instability: From the linear to the circular geometry," Phys. Fluids A **1**, 224–240 (1989).
[28]Y. Couder, N. Gerard, and M. Rabaud, "Narrow fingers in the Saffman-Taylor instability," Phys. Rev. A **34**, 5175 (1986).
[29]G. M. Homsy, "Viscous fingering in porous media," Annu. Rev. Fluid Mech. **19**, 271–311 (1987).
[30]C. A. Schneider, W. S. Rasband, and K. W. Eliceiri, "NIH image to ImageJ: 25 years of image analysis," Nat. Methods **9**, 671–675 (2012).
[31]G. Van Rossum and F. L. Drake, *Python 3 Reference Manual* (CreateSpace, Scotts Valley, CA, 2009).
[32]K. Baker and G. Sullivan, "Multiple bandpass filters in image processing," IEE Proc. E **127**, 173–184 (1980).
[33]A. W. Setiawan, T. R. Mengko, O. S. Santoso, and A. B. Suksmono, "Color retinal image enhancement using CLAHE," in *International Conference on ICT for Smart Society* (IEEE, 2013).
[34]D. Daniel, J. V. Timonen, R. Li, S. J. Velling, and J. Aizenberg, "Oleoplaning droplets on lubricated surfaces," Nat. Phys. **13**, 1020–1025 (2017).
[35]L. Limozin and K. Sengupta, "Quantitative reflection interference contrast microscopy (RICM) in soft matter and cell adhesion," ChemPhysChem **10**, 2752–2768 (2009).
[36]M. Sugiyama, H. Ogawa, K. Kitagawa, and K. Suzuki, "Single-shot surface profiling by local model fitting," Appl. Opt. **45**, 7999–8005 (2006).
[37]L. Kai and Q. Kemao, "Fast frequency-guided sequential demodulation of a single fringe pattern," Opt. Lett. **35**, 3718–3720 (2010).
[38]H. Wang and Q. Kemao, "Frequency guided methods for demodulation of a single fringe pattern," Opt. Express **17**, 15118–15127 (2009).
[39]K. Kitagawa, "Thin-film thickness profile measurement by three-wavelength interference color analysis," Appl. Opt. **52**, 1998–2007 (2013).
[40]M. Mendez, M. Balabane, and J.-M. Buchlin, "Multi-scale proper orthogonal decomposition of complex fluid flows," J. Fluid Mech. **870**, 988–1036 (2019).
[41]K. Taira, S. L. Brunton, S. T. Dawson, C. W. Rowley, T. Colonius, B. J. McKeon, O. T. Schmidt, S. Gordeyev, V. Theofilis, and L. S. Ukeiley, "Modal analysis of fluid flows: An overview," AIAA J. **55**, 4013–4041 (2017).
[42]J. N. Israelachvili, *Intermolecular and Surface Forces* (Academic Press, 2011).
[43]J. VanderPlas, *Python Data Science Handbook: Essential Tools for Working with Data* (O'Reilly Media, Inc., 2016).
[44]L. Paterson, "Radial fingering in a Hele Shaw cell," J. Fluid Mech. **113**, 513–529 (1981).